Burning plasma projections using drift-wave transport models and scalings for the H-mode pedestal

J.E. Kinsey[1], G. Bateman[1], T. Onjun[1], A.H. Kritz[1], A. Pankin[1], G.M. Staebler[2] and R.E. Waltz[2]

[1] Lehigh University, Bethlehem, PN 18015, USA

[2] General Atomics, PO Box 85608, San Diego, CA 92186, USA

Abstract

The GLF23 and multi-mode core transport models are used along with models for the H-mode pedestal to predict the fusion performance for the International Thermonuclear Experimental Reactor, Fusion Ignition Research Experiment, and IGNITOR tokamak designs. Simulations using combinations of core and pedestal models have also been compared with experimental data for H-mode profiles in DIII-D, JET, and Alcator C-Mod. Power-independent (ballooning mode limit) and power-dependent pedestal scalings lead to very different predictions when used with the core models. Although the two drift-wave transport models reproduce the core profiles in a wide variety of tokamak discharges, they differ in their projections to burning plasma experiments for the same pedestal parameters. Differences in the core transport models in their response to the ion temperature gradient (i.e. their stiffness) and impact of the power dependence of the H-mode pedestal on fusion performance predictions are discussed.

PACS numbers: 52.65.-y, 52.25.Fi, 52.55.Fa

1. Introduction

Predicting the confinement properties in future tokamaks requires an understanding of the underlying physical mechanisms responsible for transport losses. It has long been believed that drift-wave turbulent transport is the dominant mechanism responsible for the radial transport losses of particles, energy, and momentum observed in tokamaks. Since fully kinetic turbulence simulations of time-evolving plasma profiles remain impractical, reduced transport models have been derived from first principles simulations to describe the particle, heat, and momentum fluxes due to ion temperature gradient (ITG), trapped electron (TEM), and electron temperature gradient (ETG) modes. These models for 'anomalous' transport have been incorporated into various transport codes and used along with models for neoclassical transport losses due to Coulomb collisions to predict the flux-surface-averaged radial fluxes of heat, particles, and momentum.

Drift-wave based models have demonstrated a surprising level of success in predicting experimental profiles from a wide range of tokamaks [1–17]. However, in previous integrated modelling simulations, experimental data were needed to provide the temperatures, densities, and rotation near the boundary. Models for the boundary conditions are clearly needed in order to make integrated modelling codes more predictive. This is a particularly sensitive issue in predicting the fusion performance in simulations of proposed burning plasma experiments focused on high confinement (H-mode) operation. It is known that the predicted performance of fusion reactor designs (i.e. the predicted fusion power production) is sensitive to the temperature and density at the top of the H-mode pedestal. Here, it is shown that the power dependence of the pedestal height is a critical issue.

In this paper, we use the GLF23 [2] gyro-Landau-fluid and the multi-mode (MM95) [3, 4] fluid-based drift-wave transport models along with several pedestal models to predict the fusion performance in the International Thermonuclear Experimental Reactor (ITER) [18, 19], Fusion Ignition Research Experiment (FIRE) [20], and IGNITOR [21–24] burning plasma experiments. In section 2, an overview of the simulation methodology is provided including a description of GLF23 and MM95 core transport models. These are transport models that have been widely tested against experimental data. The models for the H-mode pedestal that are used in this study are also described. In section 3, results are shown where the GLF23 and MM95 transport models are used along with several pedestal models to predict the profiles that are compared with the experimental profiles from the DIII-D [25], Joint European Torus (JET) [26], and Alcator C-Mod [27]

tokamaks. In section 4, the predictions for the three burning plasma devices are described and their fusion performance is assessed. Here, we show that using different pedestal scalings coupled with the core models can lead to very different predictions for the proposed burning plasma experiments. Finally, in section 5 the consequences associated with stiffness in the core transport and the possible power dependence in the scaling of the H-mode pedestal are discussed.

2. Simulation methodology

In this section, we provide an overview of the GLF23 and MM95 core transport and H-mode pedestal models used in this study. A description of the simulation methodology used for the combined core and pedestal modelling of H-mode experimental data and burning plasma experiments is also provided.

2.1. The GLF23 transport model

The GLF23 transport model [2] uses drift-wave linear eigenmodes to compute the quasi-linear energy, toroidal momentum, and particle fluxes due to ITG/ETG and TEMs. The model differs from other drift-wave-based transport models in that it includes kinetic effects through the use of gyro-Landau-fluid equations. It also includes the effects of $E \times B$ shear flow and Shafranov shift (α) stabilization. The transport is computed using a spectrum of eigenmodes with ten wavenumbers for the ITG and TEM and ten wavenumbers for the short wavelength ETG modes. Here, the logarithmic k_y spectrum ranges from 0.02 to 0.5 for the ITG/TEM modes, with the same wavenumbers simply scaled up by the square root of the mass ratio for the ETG modes. The fluxes were originally normalized to give the same ion thermal energy flux as obtained in a set of nonlinear gyro-Landau-fluid simulations of ITG/TEM modes [2]. The norm factor was then applied to all channels of transport for both the ITG/TEM and ETG modes.

Since publication of the 1996 GLF23 model, it has been found that fully kinetic nonlinear simulations [28] predict a factor of approximately one quarter of the ITG transport that was previously predicted by gyro-Landau-fluid simulations for the plasma parameters that were used to normalize GLF23. Also, recent nonlinear simulations of ETG modes show that the electron energy flux due to ETG modes can be much larger than estimated from simply rescaling ITG results using the electron-to-ion mass ratio [29]. However, it is not yet possible to perform a fully kinetic nonlinear simulation of ETG modes with all the physics included (i.e. physics associated with both electrons and ions). It was therefore decided to determine the best fit value of the ETG mode coefficient in the model using experimental data. Since the proposed tokamak burning plasma experiments are based on the H-mode operational regime, a database of 50 H-mode discharges from JET, DIII-D, and C-Mod was used to determine the best fit value of the ETG mode coefficient. With the exception of the C-Mod discharges, most, if not all, were Type I ELMy H-mode discharges. The ETG coefficient was varied and the best fit value determined to yield a zero offset in the predicted pedestal-corrected stored energy (i.e. subtracting the stored energy outside the H-mode

pedestal boundary condition) for the data set. Compared with the original model, the normalizing coefficient for the ITG/TEM modes is reduced by a factor of 3.7 to be consistent with GYRO [30] nonlinear gyrokinetic simulations, while the ETG mode coefficient is increased by a factor of 4.8. The linear mode growth rates and frequencies are used in the quasi-linear mixing length rule for the diffusivities. The trial wavefunction is not altered by the renormalization. There is also a nonlinear $n = 0$ radial mode damping rate that also enters into the formula. The saturation levels were determined from nonlinear ITG mode gyrokinetic simulations using the GYRO code. These simulations assumed adiabatic electrons while GLF23 has TEM effects. The trapped particle effects in GLF23 were, of course, turned off for the comparisons of the ion thermal diffusivity from the GYRO runs.

Hence, the original version of the GLF23 model has been renormalized using nonlinear gyrokinetic simulations. The only difference then in this version of the model compared with the original model is that the ITG/TEM norm factor has changed and a new norm factor for the ETG modes has been introduced. The quality of the fit using the new GLF23 model is shown in figure 1. The renormalized GLF23 model has an rms error of only $\sigma_W = 8.7\%$ over the data set, which is a small improvement over the original GLF23 model ($\sigma_W = 10\%$). It is important to note that the purpose of the renormalization was not to improve agreement between the model predictions and experimental data but rather to improve agreement between the model and first principles theory i.e. turbulence simulations. Here, the rms error is defined as

$$\sigma_W = \sqrt{\frac{\sum_i (W_{mi}/W_{xi} - 1)^2}{N}}, \qquad (1)$$

where i is the discharge index, N is the total number of discharges, and $W_{m,x}$ refer to the model predicted and experimental stored energies, respectively.
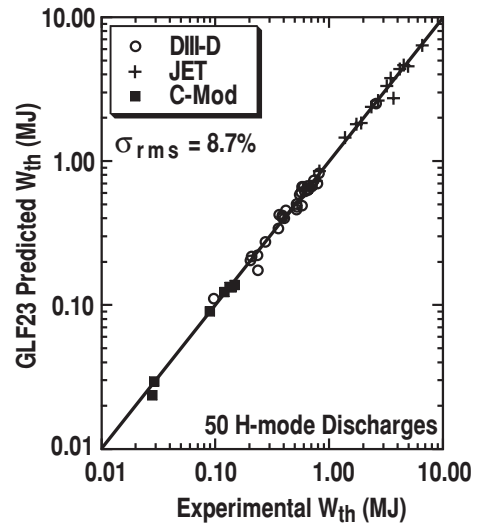

Figure 1. GLF23 predicted (renormalized) versus experimental core stored energy with boundary conditions enforced at $\hat{\rho} = 0.8$ for H-mode discharges from the DIII-D, JET, and C-Mod tokamaks.

2.2. The MM95 transport model

The MM95 transport model [3,4] is a drift-wave-based model developed in 1995 that combines the Weiland ITG/TEM model together with models for the drift-resistive and kinetic ballooning modes. The Weiland fluid-based model is a dispersion type model that computes the quasi-linear energy and particle fluxes due to ITG and TEM modes. It includes the effects of impurities, parallel ion motion, finite Larmor radius, and finite β in the strong ballooning approximation, as described in [3]. The effective radial diffusivities are computed from the linear eigenmodes assuming a single wavenumber, $k_\theta \rho_s = 0.316$, and a mixing length rule of the form

$$\chi \propto \frac{\gamma^3/k_x^2}{(\omega - (5/3)\omega_D)^2 + \gamma^2}, \qquad (2)$$

where γ is the mode growth rate, ω is the mode frequency, ω_D is the diamagnetic drift frequency, and k_x is the radial wavenumber. As described in reference [3], all the anomalous transport contributions in the MM95 model include the factor κ^{-4}, where κ is the elongation (height divided by width) of each local flux surface. The MM95 model has included this elongation factor in all the comparisons that have been made between the results of simulations and experimental data [5, 11–15]. Previous simulations using the MM95 model in the BALDUR code have yielded average rms errors in the stored energy of H-mode discharges in the range 10–15% with corresponding errors in the density and temperature profiles of less than 20% [5, 13, 14, 31].

2.3. Models for the H-mode pedestal

Recently, the International Tokamak Physics Activity (ITPA) H-mode and Pedestal Database groups [32–35] have assembled a common database of ELMy H-mode tokamak discharges containing both pedestal and core stored energy data as well as pedestal temperatures, densities, and other plasma parameters. Utilizing these data, empirical models have been developed to predict the temperature and density at the top of the pedestal near the edge of H-mode plasmas. In an effort to enhance our predictive capability of tokamak confinement, these pedestal models have been implemented in transport codes to provide predictive boundary conditions for integrated modelling simulations. The pedestal models can be broken into two types. One type consists of magnetohydrodynamic (MHD) limit models, where it is assumed that the pressure gradient in the pedestal region is determined by MHD stability limits. Another type of pedestal model, sometimes called a thermal conduction model, assumes that thermal conduction losses are the dominant loss mechanisms in the pedestal and that thermal losses associated with ELM activity are comparatively smaller. One important difference between these two types of pedestal models is that MHD limit models are power-independent, whereas the thermal conduction models tend to have a loss power dependence.

In this paper, an MHD limit pedestal model is constructed that assumes that the edge pressure gradient is limited by high-n ideal MHD ballooning modes and the pedestal width is proportional to the major radius times the square root of poloidal beta, $\Delta \propto R\sqrt{\beta_p}$ [36]. The safety factor and magnetic shear that are used in the ballooning mode limit are computed one pedestal width from the separatrix and are reduced by the effect of the bootstrap current. The pedestal temperature model is calibrated using 533 data points from the International Pedestal Database (v.3.1) based on experimental data from JT-60U, ASDEX-U, JET, and DIII-D. The formula for the pedestal temperature is given by

$$T_{\text{ped}} = 0.034 \left(\frac{B_T}{q}\right)^4 \left[\frac{a(1+\kappa_{95})}{I_p}\right]^2 \left(\frac{\alpha_c^2}{n_{\text{ped}}}\right), \qquad (3)$$

where B_T is the toroidal field (T), q is the safety factor at the top of the pedestal, a is the plasma minor radius (m), I_p is the plasma current (MA), n_{ped} is the pedestal density in 10^{20} m^{-3}, and α_c is the critical MHD α parameter. Here, α_c is given by

$$\alpha_c = 0.4\hat{s}[1 + \kappa_{95}^2(1 + 5\delta_{95}^2)], \qquad (4)$$

where $\hat{s}$ is the magnetic shear and κ_{95} and δ_{95} are the elongation and triangularity at the 95% flux surface. It should be noted that equation (3) is a nonlinear equation for T_{ped} since the safety factor and magnetic shear are computed one pedestal width, Δ, from the separatrix, and Δ is itself a function of T_{ped} [36]. The safety factor has a logarithmic singularity at the separatrix and, in addition, the magnetic shear in the steep gradient region of the pedestal is reduced by the effect of the bootstrap current. This model, shown in figure 2(a), has an rms error of 32.9%. The same data yield an empirical model for the pedestal density proportional to the line-averaged density ($n_{\text{ped}} = 0.71\bar{n}_e$), which has an rms error of 12.1%, as shown in figure 2(b). Other models for the pedestal temperature based on the pressure gradient limited by high-n ballooning modes and different scalings for the pedestal width are described in [36].

The other pedestal models considered in this paper include two power-dependent models constructed by the ITPA Confinement and Pedestal Database groups. The first model follows from a free-fit to 444 observations from seven tokamaks and satisfies the Kadomstev constraint [31, 37]. The formula for the pedestal stored energy corresponds to equation (2) given in [38],

$$W_{\text{ped1}} = 0.000\,73 I^{1.45\pm0.11} R^{1.54\pm0.14} P^{0.16\pm0.03} \bar{n}^{0.08\pm0.05}$$
$$\times B^{0.32\pm0.09} \kappa_a^{1.78\pm0.19} \epsilon^{-1.74\pm0.29} M^{0.2} F_q^{2.27\pm0.20}, \quad (5)$$

where I is the plasma current (MA), R is the major radius (m), P is the thermal loss power (MW), $\bar{n}$ is the average electron density (10^{-19} m^{-3}), B is the toroidal field (T), κ_a is the elongation at the last closed flux surface, ϵ is the inverse aspect ratio, M is the atomic mass, and F_q is a shaping factor (q_{95}/q_{cyl}). Here, q_{cyl} is defined as $(5\kappa_a a^2 B)/(RI)$. The other power-dependent formula (equation (3) in [38]) follows from an elimination of Type III ELMy data and is given by

$$W_{\text{ped2}} = 0.014 I^{1.60\pm0.06} R^{1.36\pm0.09} P^{0.29\pm0.03} \bar{n}^{-0.07\pm0.04}$$
$$\times B^{0.31\pm0.05} M^{0.2} F_q^{2.34\pm0.17}. \qquad (6)$$

It should be noted that this formula has a stronger power dependence than W_{ped1} and lacks any dependence on inverse aspect ratio and elongation.
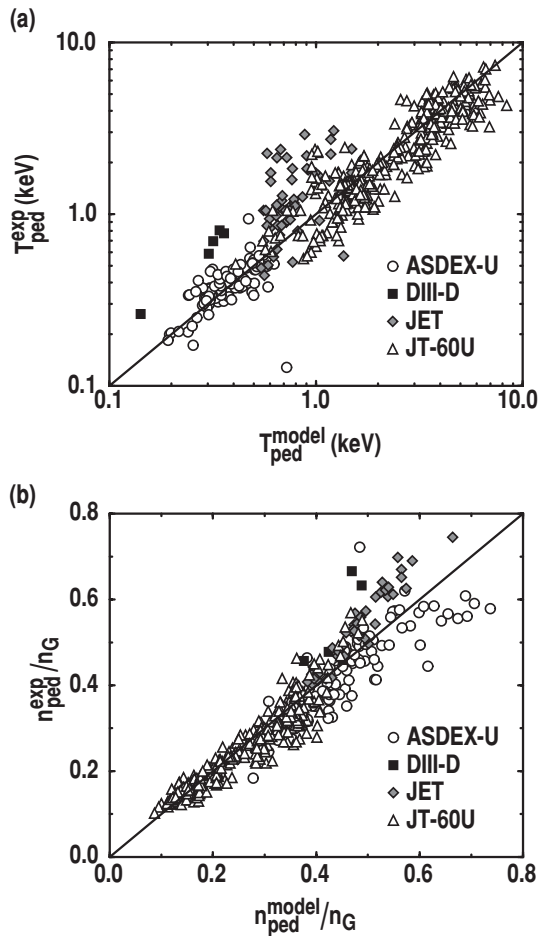
Figure 2. (*a*) Pedestal temperatures from the International Profile Database [1] compared with the $R\sqrt{\beta_p}$ model predictions. (*b*) Pedestal densities from the database compared with the model $n_{\text{ped}} = 0.71\bar{n}_e$.

2.4. Combined core transport and pedestal modelling methodology

The results obtained using the renormalized GLF23 transport model were carried out using the XPTOR transport code [6]. For the combined core and pedestal modelling of experimental H-mode discharges, the temperature profiles were predicted while taking the density, toroidal rotation, and safety factor profiles from experimental analyses. The equilibrium data, sources, and sinks were obtained from an experimental power balance analysis carried out using the TRANSP [40] or ONETWO [41] code. The boundary conditions were enforced at a normalized radius of $\hat{\rho} = 0.85$. Here, $\hat{\rho} = \rho/\rho(a)$ is the normalized toroidal flux and a is the minor radius. When the pedestal models were employed, the values for T_{ped} were computed from the pedestal scalings, taking n_{ped} from the experimental data at $\hat{\rho} = 0.85$. The effects of $\boldsymbol{E} \times \boldsymbol{B}$ shear and Shafranov shift stabilization were computed using the model-predicted temperature profiles. The poloidal velocity was computed using a collisionless neoclassical estimate [42].

In the burning plasma simulations using the GLF23 model, the temperature profiles were evolved to steady-state holding the plasma geometry, safety factor profile, density profiles, effective charge, Z_{eff}, and auxiliary heating power deposition profiles fixed in time. For simplicity, we assumed the same elongation and triangularity, monotonic safety factor, and density profile shape for the three burning plasma devices to facilitate a uniform assessment. The Z_{eff} profile was assumed to be flat, and carbon was the only impurity included. The sources and sinks due to Ohmic heating, alpha heating, and radiation were self-consistently computed using the model-predicted temperature profiles. While no toroidal rotation was assumed for ITER, FIRE, or IGNITOR, the poloidal velocity and pressure gradient terms in the radial electric field still contributed. Overall, the $\boldsymbol{E} \times \boldsymbol{B}$ shear effects were found to be small. For the Ohmic heating power, we assumed a fixed current density profile and used the neoclassical resistivity given by Hirshman *et al* [43]. For the radiative losses we computed the bremsstrahlung radiation from the NRL plasma formulary [44] and synchrotron radiation by Trubnikov [45] assuming that 50% of the radiation is reflected by the walls and absorbed in the plasma. No sawteeth or any other MHD activity were considered in the GLF23 simulations. The boundary conditions were enforced at a normalized toroidal flux of $\hat{\rho} = 0.95$. For the density profile, we used a mildly peaked profile with the electron density at $\hat{\rho} = 0.95$ equal to 85% of the line-averaged electron density. The electron density profile was obtained from a fit to the predicted density profile from BALDUR simulations using the MM95 model.

The results obtained using the MM95 transport model were carried out using the BALDUR transport code [46]. The BALDUR predictive integrated modelling code contains a variety of modules for computing sources, sinks, transport, boundary conditions, and the effects of large-scale instabilities. Profiles are predicted as a function of radius and time for the electron temperature, ion temperature, hydrogenic and impurity ion and neutral particle densities, electron density, magnetic q, Ohmic heating, alpha heating, distribution of fast alpha particles, and shapes of the magnetic flux surfaces. In addition, the effect that periodic sawtooth crashes have on all the axisymmetry profiles are computed, including fast ions. Here, we examined the steady-state profiles after sawteeth have been turned off.

In MM95 simulations with the BALDUR code, input values are prescribed as a function of time for the shape of the plasma boundary, the plasma current, the toroidal magnetic field at the boundary, the line- or volume-average electron density, the relative impurity ion densities at the boundary, and, in the case of radio frequency heating, the auxiliary heating power profile. In the case of neutral beam injection (NBI) heating, input values are used to describe the geometry of the beam line, the energy and isotope of the neutrals, the full, half, and third fractions of the neutrals, and the power passing through the boundary of the plasma. During the Ohmic and L-mode stages of each simulation, the electron and ion temperatures, as well as all the ion densities, must be prescribed at the boundary of the simulation. During the H-mode stage of each simulation, only the relative concentrations of hydrogen isotope and impurity densities are prescribed, while the electron density and the electron and ion temperatures are predicted from the pedestal model.

In simulations of existing tokamak experiments using the MM95 model, the simulation boundary is placed at the top of

Table 1. Reference design parameters for the ITER, FIRE, and IGNITOR tokamaks.

Device	ITER	FIRE	IGNITOR
R_0 (m)	6.20	2.14	1.32
a (m)	2.00	0.60	0.45
κ_a	1.78	1.80	1.80
δ	0.40	0.40	0.40
B_T (T)	5.30	10.0	13.0
I_p (MA)	15.0	7.70	9.0
q_{95}	3.0	3.0	3.0
$\bar{n}_e (10^{20}\,\mathrm{m}^{-3})$	1.03	5.88	8.69
$\bar{n}_e/n_G$	0.85	0.70	0.60
$\bar{Z}_{eff}$	1.50	1.40	1.20
$V\,(\mathrm{m}^3)$	830	27.0	9.50
P_{aux} (MW)	40.0	20.0	10.0
P_{LH} (MW)	49.2	26.3	22.2

the electron density pedestal, which is generally more clearly defined than the electron or ion temperature pedestals. In simulations of ITER, FIRE, and IGNITOR, the simulation boundary is placed at the minor radius given in table 1. In the ITER simulations, there is a ramp in the plasma current, density, and auxiliary heating power during the first 20 s. Sawtooth oscillations are turned off at 295 s in order to provide reproducibly steady-state conditions at 300 s, which is used as the diagnostic time. The impurity concentration at the boundary of the ITER simulations is taken to be 2% beryllium, 0.12% argon [19], and 0.1% helium. In the FIRE simulations, the current and density ramps occur during the first 7 s, sawtooth oscillations are turned off at 19 s, and the diagnostic time is at 21 s. The impurity concentration at the boundary of the FIRE simulations is taken to be 3% beryllium. In the IGNITOR simulations, the current and density ramps occur during the first 4 s, sawtooth oscillations are turned off at 7 s, and the diagnostic time is at 8 s. The impurity concentration at the boundary of the IGNITOR simulations is taken to be 1.7% beryllium. For the three devices, the impurity concentration levels yielded Z_{eff} values of 1.5, 1.4, and 1.2 for ITER, FIRE, and IGNITOR, respectively, to allow uniform comparison with the GLF23 results. Beryllium coating of the first wall is assumed for all three devices [18, 20, 21]. The reason that sawtooth oscillations are turned off before the diagnostic time is that a transient in the alpha power delivered to thermal electrons and ions is observed after each sawtooth crash in the BALDUR simulations. Steady-state profiles were desired so that uniform comparisons with the GLF23 results could be made. During the fusion burn, a helium concentration of less than about 2% accumulates within the plasma of each device.

The BALDUR code, using the MM95 transport model, predicts the time evolution of the ion density profiles for deuterium, tritium, helium, and the impurities. In the simulations of ITER, for example, the impurities are beryllium, argon, and helium. At the boundary of the ITER simulations (that is, at the top of the pedestal), the beryllium density is prescribed to be 2% of the electron density, the argon density is 0.12% of the electron density, and the helium density is 0.10% of the electron density, and equal densities are prescribed for the deuterium and tritium ions. At the end of the ITER simulation (after 300 s), it is found that the central helium density builds up to about 1.8% of the central electron density, while the central beryllium density is 1.5% and the central

argon density is 0.07%. In the FIRE simulations, the beryllium density at the edge of each simulation is prescribed to be 3% of the electron density, while the helium density is 0.1% and there are no other impurities. At the end of the FIRE simulations, the central beryllium is found to be about 2.4% of the central electron density and the central helium accumulation remains below 0.5%. In the IGNITOR simulations, the edge beryllium density is specified to be 1.7% and the helium density to be 0.1% of the edge electron density. At the end of the IGNITOR simulations, the central beryllium density is approximately 1.5% and the helium density remains below 0.4% of the electron density.

Although the BALDUR code follows the time evolution of the individual ion density profiles for deuterium, tritium, and each of the impurity species, the MM95 model, in terms of transport, considers only a single aggregate hydrogenic species and a single aggregate impurity species. Input parameters for the MM95 model at each radius, such as the ion charge or mass, are computed as density-weighted averages over the individual hydrogenic or impurity ion species. The MM95 model computes a single particle transport coefficient for the hydrogenic ions and a single coefficient for the impurity ions. The density profiles of the individual hydrogenic and impurity species evolve independently in response to the different sources, sinks, and boundary conditions for the different species, as well as transport and the effect of sawtooth oscillations.

Note that the GLF23 has been calibrated against experimental data using the XPTOR code, but not in the BALDUR code. Conversely, the MM95 model has been calibrated against experimental data most extensively using the BALDUR code. Consequently, in simulations of burning plasma experiments, each model has been calibrated in the code in which the model has been validated.

3. Transport simulations of experimental data using pedestal scaling boundary conditions

In the past, predictive integrated modelling simulations have generally been performed using experimental data to determine the boundary conditions for the density, temperature, and toroidal rotation profiles. This limits the overall predictive capability of the simulations. This issue is particularly important when considering fusion reactor performance involving H-mode plasmas, since the predicted fusion power is sensitive to the temperature and density boundary conditions that are assumed at the top of the pedestal. The MHD limit pedestal model described above (equations (3) and (4)) has been used to provide the boundary conditions in simulations of DIII-D and JET H-mode discharges using the MM95 model in the BALDUR code [46]. It is found that the overall agreement between the simulated profiles and experimental data using that pedestal model is approximately 10% (figure 3), which is nearly the same as the level of agreement obtained when the boundary conditions are prescribed using experimental data. The discharges used in figure 3 are described in [11]. Figure 3 provides a benchmark comparison with experimental data for the combination of the MHD limit pedestal model together with the MM95 core transport model in the BALDUR integrated modelling code.
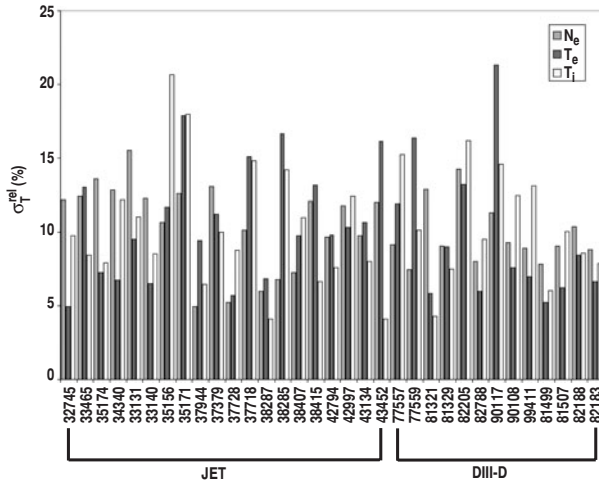
Figure 3. Relative rms error between the simulation and experimental density and temperature profiles for 33 H-mode discharges using the MM95 model together with the Sugihara power-independent MHD limited pedestal model [36].
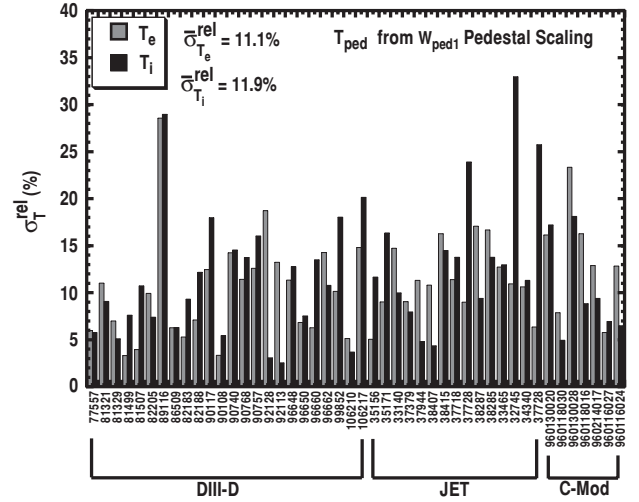

Figure 4. (*a*) Predicted versus experimental pedestal temperature using the power-dependent pedestal scaling W_{ped1} from [38] for 47 H-mode discharges. (*b*) Predicted versus experimental core stored energy using the renormalized GLF23 model with pedestal scaling boundary conditions.

A similar exercise has been carried out using the renormalized GLF23 model together with the pedestal scalings described in the previous section from [38]. The results of simulations using the GLF23 core transport model together with the power-dependent thermal conduction pedestal scaling (W_{ped1}) to provide T_{ped} are shown in figure 4.

For the 47 H-mode shots shown in figure 4(*a*), the power-dependent scaling has a 33% rms deviation between the predicted and experimental values for T_{ped}. Using T_{ped} from this pedestal scaling to set the boundary conditions for T_e and T_i in the simulations with the GLF23 model yields an rms error, σ_W, of 20% in the core stored energy as shown in figure 4(*b*). Using the power-dependent pedestal scaling, W_{ped2}, found by eliminating Type III ELMy data results in a slightly higher rms error, σ_W, of 23% in the core stored energy. Here, the rms error is defined as $[(1/N)\sum(W_s/W_x - 1)^2]^{0.5}$, where W_s and W_x are the simulated and experimental stored energies and N is the number of discharges. The average rms error for the temperature profiles relative to the maximum experimental temperature in each profile is 11.5%. The rms error is shown for each discharge in figure 5. Here, the

Figure 5. Relative rms error between the simulation and experimental temperature profiles for 47 H-mode discharges using the renormed GLF23 model along with the power-dependent pedestal model (W_{ped1}).
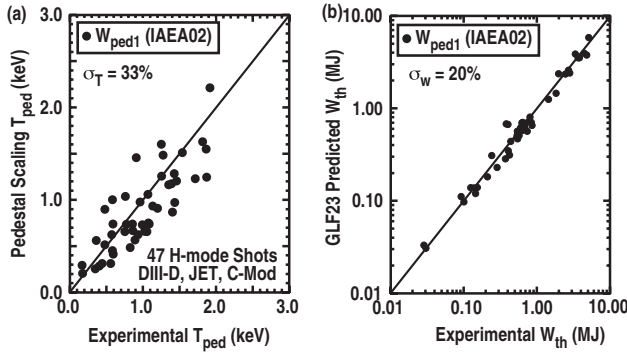
boundary conditions were enforced at a normalized radius of $\hat{\rho} = 0.85$. While this may be inside the actual top of the pedestal, $\hat{\rho} = 0.85$ was used to insure that GLF23 was not used in the steep gradient pedestal region where it is not applicable. To compensate for this in the pedestal scalings W_{ped1} and W_{ped2}, the value of T_{ped} was enhanced by a factor of $C_{ped} = 1.25$ so that a nearly zero offset in the error in T_{ped} resulted. In simulations of the 47 H-mode discharges, including C_{ped} changed the average $(1/N)\sum(T_s/T_x)$ in the predicted T_{ped} from 0.75 to 0.95 keV when the pedestal scaling W_{ped1} was used. Including $C_{ped} = 1.25$ in the simulations also yields close to a zero offset in the error in the GLF23 predicted core stored energy from simulations using the pedestal scaling boundary conditions W_{ped1}. Figure 4 provides a benchmark comparison with experimental data for the combination of the power-dependent pedestal model together with the GLF23 core transport model in the XPTOR code.

4. Burning plasma projections

The renormalized GLF23 and the original MM95 models have been applied in simulations of the ITER, FIRE, and IGNITOR designs. The design parameters for these burning plasma experiments are given in table 1. The predicted fusion performance, $Q = 5P_\alpha/(P_{aux} + P_{ohm})$, from simulations using the GLF23 and MM95 models are shown in figure 6 as a function of pedestal temperature assuming a fixed pedestal density, where $n_{ped} = 0.71\bar{n}_e$ and $\bar{n}_e/n_G = 0.85$, 0.70, and 0.60, respectively, for ITER, FIRE, and IGNITOR. Here, P_α is the alpha heating power, P_{aux} is the auxiliary heating power, P_{ohm} is the Ohmic heating power, and $n_G = I_p/(\pi a^2)$. It is observed that the fusion Q increases with pedestal temperature at fixed plasma density. In general, the renormalized GLF23 model results show a stronger sensitivity for the fusion Q as a function of the pedestal temperature due to the stiff nature of the model. For ITER, the fusion Q scales as $T_{ped}^{1.8}$ using the GLF23 model and as $T_{ped}^{0.6}$ using the MM95 model. While
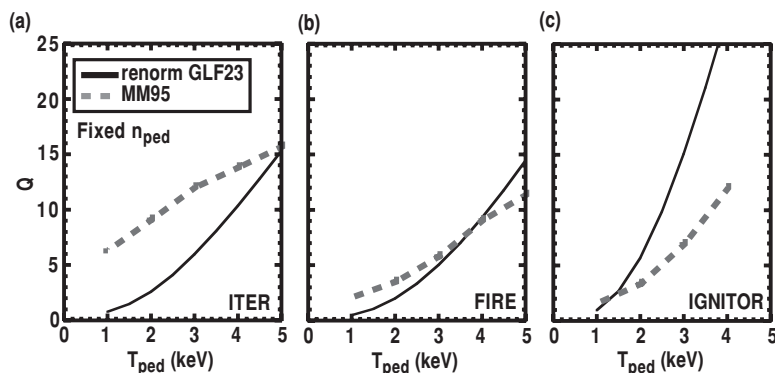
Figure 6. Fusion Q predicted using MM95 and GLF23 models versus pedestal temperature for (*a*) ITER, (*b*) FIRE, and (*c*) IGNITOR with fixed pedestal density and auxiliary heating power for each device given in table 1.
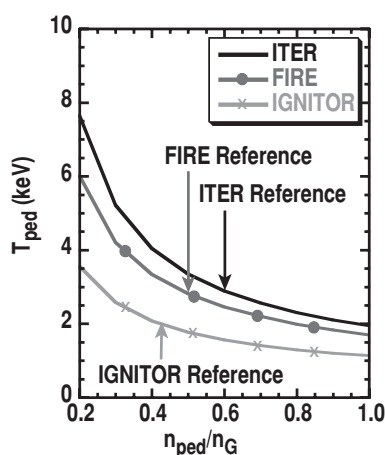

Figure 7. Predicted pedestal temperature versus pedestal density divided by the Greenwald density, n_{G}, for ITER, FIRE, and IGNITOR using the $R\sqrt{\beta_p}$ MHD limit pedestal model. The reference densities are indicated with arrows.

the FIRE predictions from the two models are similar, the renormalized GLF23 and MM95 models yield very different predictions at low pedestal temperatures for ITER and at high pedestal temperatures for IGNITOR.

Plotting Q versus T_{ped} at fixed n_{ped} is misleading, however, since the MHD limit (power-independent) $R\sqrt{\beta_p}$ pedestal model indicates that pedestal temperature is inversely related to pedestal density, as shown in figure 7, and the pedestal density is proportional to the core density. Hence, an increase in the plasma density causes a decrease in the pedestal temperature, which can offset the gain in fusion power. The pedestal temperatures predicted by this model at the design densities are 2.89 keV, 2.82 keV, and 1.98 keV for ITER, FIRE, and IGNITOR, respectively.

Figure 8 shows the resulting fusion Q as a function of normalized plasma density for simulations of ITER, FIRE, and IGNITOR using the renormalized GLF23 and MM95 models together with the $R\sqrt{\beta_p}$ and the power-dependent (W_{ped1}) pedestal models. The results obtained using the power-dependent pedestal model (solid lines) lead to more optimistic predictions than those obtained using the MHD limit pedestal model (dashed lines) due to higher values of T_{ped} predicted by the power-dependent pedestal model. The differences in predicted fusion Q for a given core model are

largely due to differences in the power dependence in the two pedestal models. The GLF23 and MM95 results for ITER are closer together when the power-dependent pedestal scaling is used because the values of T_{ped} are higher (figure 6). At the reference densities, the values for β_{ped}^{N} ($\beta_{ped}/(I/aB)$) are approximately 0.9, 1.3, and 0.6 for ITER, FIRE, and IGNITOR, respectively, when the GLF23 and MM95 models are used along with the power-dependent pedestal scaling (equation (2) in [6]). These results also depend on the total heating power. This issue is discussed in the following sections.

Simulations using the MM95 core transport model together with another pedestal temperature model, in which the pedestal pressure gradient is limited by high-n ballooning modes and the width scales with the gyro-radius times magnetic shear squared, yield very similar results, as described in [39]. In that paper, the sensitivity of the results to a variation over one standard deviation of the pedestal model was studied. It was found in that paper [39] that the fusion Q varies up or down by only two or three units (e.g. between 9 and 13, in the case of ITER) as the pedestal model is varied from one standard deviation above to one standard deviation below the baseline model.

5. Temperature profile stiffness

As shown in the previous section, the predicted fusion Q from the GLF23 and MM95 transport models can be very different. We have conjectured that this difference is attributed to differing levels of stiffness in the transport models, with the GLF23 model being more stiff than the MM95 model. By stiffness we mean the rate at which the transport fluxes increase as a function of the logarithmic temperature gradient once a critical value is exceeded. Two key properties associated with stiff models are that the profiles are unresponsive to additional heating power and that the predicted central temperature is sensitive to the boundary (i.e. pedestal) temperature. This translates into Q being sensitive to both P_{aux} and T_{ped}.

In order to understand why the two models yield different values for the fusion Q, scans in logarithmic temperature gradient were conducted for low and high T_{ped} cases at several different radii using the parameters listed in table 1 for ITER. For this exercise, the predicted temperature profiles from GLF23 simulations of ITER at $T_{ped} = 2.5$ and 5.0 keV were
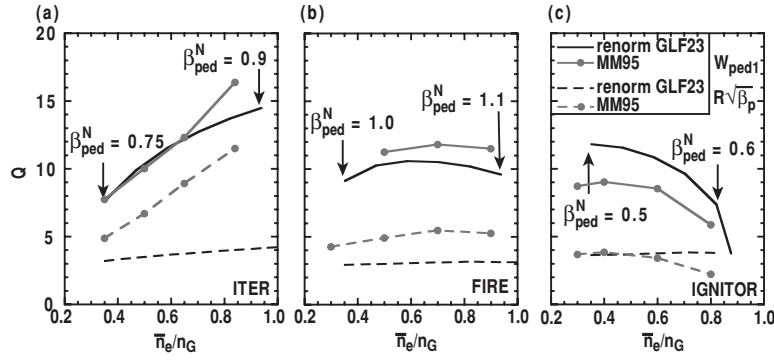
Figure 8. Fusion Q predicted using the MM95 and renormed GLF23 models versus line-averaged electron density divided by the Greenwald density for (*a*) ITER, (*b*) FIRE, and (*c*) IGNITOR assuming T_{ped} varies with density according to the power-dependent (——) and $R\sqrt{\beta_p}$ MHD limit (- - - -) pedestal models.
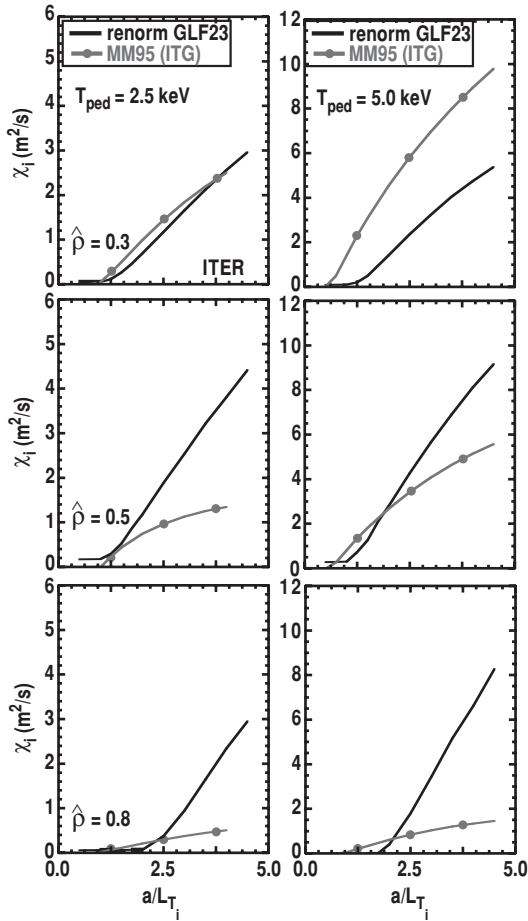

Figure 9. Predicted ion thermal diffusivity versus logarithmic ITG, a/L_{T_i}, for ITER with fixed pedestal temperatures of 2.5 keV (left panels) and 5.0 keV (right panels) using the renormed GLF23 model (——) and MM95 model (— · —). Results are shown at three normalized radii, $\hat{\rho} = 0.3$ (top panels), 0.5 (middle panels), and 0.8 (bottom panels).

taken and used as input profiles for both models in the XPTOR code [6]. The ion thermal diffusivities computed using the GLF23 and MM95 models were then plotted as a function of the logarithmic temperature gradient, a/L_{T_i}, was varied, with all other plasma parameters taken from the prescribed profiles. Figure 9 illustrates χ_i versus a/L_{T_i} for ITER with

$T_{ped} = 2.5$ keV (left panels) and 5.0 keV (right panels) using the GLF23 and MM95 models at three different radii.

The differences in stiffness for the ITG/TEM transport are clearly evident at large radii. For example, at $\hat{\rho} = 0.8$ the MM95 model χ_i varies much less with a/L_{T_i}. This weakening in stiffness with radius is due to the κ^{-4} factor included in the MM95 diffusivity. This factor is, of course, more important at larger radii where the local elongation is larger. The resulting impact is that higher temperature gradients can be attained at large radii with little increase in χ_i computed using the MM95 model. By comparision, the temperature profiles are constrained to lower gradients at large radii when the GLF23 model is used. For lower pedestal temperatures, the diffusivities from the two models are similar at small radii. So, the reason why GLF23 results have a lower fusion Q in ITER for $T_{ped} = 2.5$ keV is due to the comparatively larger heat diffusivity at large radii. Carefully designed experiments are clearly needed in order to test the stiffness of the ion transport in the models in the outer half of the plasma. For higher pedestal temperatures, the MM95 ITG/TEM χ_i is larger than the GLF23 χ_i. This is partly due to the finite β effects in the ITG/TEM part of the MM95 model. At $T_{ped} = 5.0$ keV, the ideal ballooning mode limit (derived in circular geometry) is approached in the Weiland ITG/TEM part of the MM95 model, causing χ_i to increase rapidly with β. The kinetic ballooning mode transport in the MM95 model also becomes large. So, while the MM95 χ_i is smaller than the GLF23 χ_i at large radii, the opposite is true at small radii. As a result, the MM95 temperature profiles for higher T_{ped} cases are broader than the GLF23 temperature profiles but yield roughly the same integrated fusion power, given similar density profiles.

As a result of differing levels of stiffness, the GLF23 and MM95 models exhibit noticeably different sensitivities of the fusion Q to changes in P_{aux} and T_{ped}. An important characteristic of a stiff model is that the temperature profiles will be insensitive to additional levels of auxiliary heating power. As a result, the fusion Q can vary enormously and as a consequence be a misleading figure of merit. Figure 10 shows the predicted fusion Q versus auxiliary heating power, P_{aux}, for ITER with $T_{ped} = 3.0$ keV using the renormed GLF23 and MM95 models. Here, only P_{aux} was varied and all other quantities were held fixed, including the pedestal conditions. For ITER, simulations using the GLF23 model yield Q varying
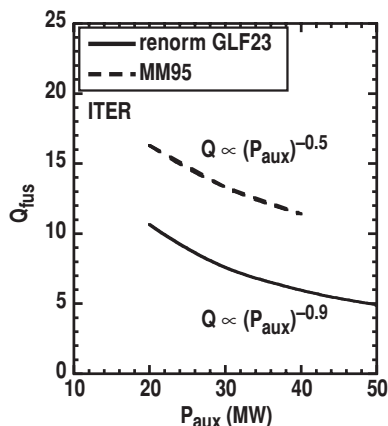
Figure 10. Predicted fusion Q versus auxiliary heating power for ITER with fixed $T_{\text{ped}} = 3.0\,\text{keV}$ using the renormed GLF23 model (——) and MM95 model (- - - -).

as $P_{\text{aux}}^{-0.9}$, while simulations using the MM95 model yield Q varying as $P_{\text{aux}}^{-0.5}$. For a perfectly stiff model, the fusion power would be independent of P_{aux}, and Q would vary as P_{aux}^{-1}. For H-mode operation, it is important to note that the heating power needs to be consistent with the power flow needed to sustain the pedestal. So, one cannot simply reduce P_{aux} arbitrarily to obtain any desired fusion Q.

If the core turbulent transport in tokamaks is indeed stiff (i.e. similar to GLF23), then one could conclude that this stiffness is a serious limitation on the fusion performance in future devices. As a result, the temperature profiles will be constrained to marginality and any attempt to add additional auxiliary heating power to increase the temperature profiles will only result in larger transport levels and lower fusion gains. However, if the H-mode pedestal height has a power dependence, then a stiff core is advantageous since it allows the plasma core to bootstrap the pedestal temperature to higher values than what could be attained if the core were only weakly stiff. With a stiff core, any incremental increase in T_{ped} would result in a similar increase in the central temperature and the fusion power. The loss power would then increase and would cause T_{ped} to rise. The feedback cycle continues until the pedestal becomes MHD limited. Ultimately, the question boils down to being able to predict when the H-mode pedestal height makes a transition from being power-dependent to being power-independent (or nearly so) and limited by MHD stability.

6. Conclusions

The GLF23 (renormed) and MM95 core transport models have been used together with models for the height of the H-mode pedestal to predict the fusion performance of the proposed ITER, FIRE, and IGNITOR burning plasma experiments during H-mode operation. The renormalized GLF23 model demonstrates a stronger sensitivity to the pedestal temperature and generally leads to more pessimistic projections than the MM95 model for all three devices when MHD limit pedestal models are used. However, because of the stiff nature of the GLF23 model, the fusion gain is strongly dependent on the auxiliary power ($Q \propto P_{\text{aux}}^{-0.9}$). The MM95 model is less stiff

and the fusion gain is less sensitive to the auxiliary power, with Q scaling approximately as $P_{\text{aux}}^{-0.5}$. Comparing the transport simulations using the pedestal models to provide the boundary conditions for T_{ped}, we find that the results obtained using a power-dependent pedestal model are strikingly different from those when a power-independent MHD limit pedestal model is used. Using a combination of the GLF23 core transport model along with an MHD type pedestal model, where the pedestal width scales as $R\sqrt{\beta_{\text{p}}}$, yields fusion gains of less than 5 for ITER, FIRE, and IGNITOR for densities in the range 0.3–0.8 times the Greenwald limit, n_{G}. Simulations of FIRE and IGNITOR using the MM95 model along with the $R\sqrt{\beta_{\text{p}}}$ pedestal model are nearly as pessimistic as the GLF23 results for FIRE and IGNITOR, but the fusion Q for ITER is noticeably higher and shows a strong sensitivity to $n_{\text{e}}/n_{\text{G}}$. On the other hand, simulations using the core models with the power-dependent pedestal scaling show more optimistic predictions. Clearly, the power dependence of the pedestal needs to be identified, and carefully designed experiments from different tokamaks would likely aid in resolving this issue.

The same combinations of core and pedestal models have also been used to predict the temperature profiles in a wide variety of H-mode discharges from the DIII-D, JET, and C-Mod tokamaks. For a set of 47 H-mode discharges, an average relative rms error of 11.5% in the temperature profiles is obtained when the renormed GLF23 model is used along with a recently developed power-dependent pedestal model to provide the boundary conditions. The corresponding rms error in the core stored energy is 20%, which is 10% higher than the rms error obtained when experimental boundary conditions are used. A similar exercise using the MM95 model along with an MHD type pedestal scaling shows little change in the average rms error (about 10%) for the profiles compared with the results obtained when experimental boundary conditions are used. The difference in sensitivity to the pedestal temperature between the models is due to the differing levels of stiffness.

For a given set of pedestal parameters, differences in the predicted fusion Q using the GLF23 and MM95 models can be attributed largely to differences in the stiffness of the ITG transport. For large radii where the local elongation is larger, the κ^{-4} reduction factor on the MM95 diffusivities significantly reduces the stiffness in the MM95 ITG mode-driven transport. For low to moderate β values, this results in higher predicted temperatures and, therefore, higher fusion gains. For several pedestal temperatures in ITER at the reference density, we find little difference in the critical gradient between the models. At high plasma β values, the predicted fusion Q using the MM95 model tends to approach the values found using the GLF23 model, owing to the β enhancements of the transport. Finite β effects in the Weiland ITG/TEM part of the MM95 model cause the transport to rise rapidly once the ideal ballooning model limit (derived for circular geometry) is exceeded. Finite β effects are not used in the GLF23 model. In addition to the β-enhanced ITG transport, there is an additional component originating from the kinetic ballooning mode transport present in the MM95 model that can be significant at moderate-to-high plasma β values. As a result, the enhanced transport at high β compensates for the model being less stiff, yielding fusion Q values similar to values predicted by GLF23.

Acknowledgments

References

[1] The 1D Modelling Working Group 2000 *Nucl. Fusion* **40** 1955
[2] Waltz R.E., Staebler G.M., Dorland W., Hammett G.W., Kotschenreuther M. and Konings J.A. 1997 *Phys. Plasmas* **4** 2482
[3] Bateman G., Kritz A.H., Kinsey J.E., Redd A.J. and Weiland J. 1998 *Phys. Plasmas* **5** 1793
[4] Kinsey J.E. and Bateman G. 1996 *Phys. Plasmas* **3** 3344
[5] Kinsey J.E., Schissel D.P. and Waltz R.E. 1997 Transport model testing and comparisons using the ITER and DIII-D profile database *24th European Conf. on Controlled Fusion and Plasma Physics* vol 21A (part III) (*Europhys. Conf. Abstracts*) (Petit-Lancy, Berchtesgaden European Physical Society) p 1081
[6] Kinsey J.E., Staebler G.M. and Waltz R.E. 2002 *Phys. Plasmas* **9** 1676
[7] Petty C.C., Wade M.R., Kinsey J.E., Baker D.R. and Luce T.C. 2002 *Phys. Plasmas* **9** 128
[8] Staebler G.M., Waltz R.E., Kinsey J.E., Bateman G., Kritz A.H., Onjun T., Pankin A., Zhu P. and Horton W. 2001 *Nucl. Fusion* **41** 891
[9] Kinsey J.E., Staebler G.M., Burrell K.H., Austin M.E. and Waltz R.E. 2001 *Phys. Rev. Lett.* **86** 814
[10] Petty C., Wade M.R., Kinsey J.E., Groebner R.J., Luce T.C. and Staebler G.M. 1999 *Phys. Rev. Lett.* **83** 3661
[11] Hannum D., Bateman G., Kinsey J., Kritz H., Onjun T. and Pankin A. 2001 *Phys. Plasmas* **8** 964
[12] Onjun T., Bateman G., Kritz A.H. and Hannum D. 2001 *Phys. Plasmas* **8** 975
[13] Pankin A., Bateman G., Kritz A., Greenwald M., Snipes J. and Fredian T. 2001 *Phys. Plasmas* **8** 4403
[14] Kinsey J.E. 1999 *Nucl. Fusion* **39** 539
[15] Bateman G., Kritz A.H., Parail V.V., Cordey J.G. and the JET Team 1999 *Phys. Plasmas* **6** 4607
[16] Kinsey J.E., Bateman G., Kritz A.H. and Redd A. 1996 *Phys. Plasmas* **3** 561
[17] Kotschenreuther M., Dorland W., Beer M.A. and Hammett G.W. 1995 *Phys. Plasmas* **2** 2381
[18] Campbell D.J. 2001 *Phys. Plasmas* **8** 2041
[19] Shimomura Y. *et al* 2001 *Nucl. Fusion* **41** 309
[20] Meade D.M. *et al* 2000 Mission and design of the fusion ignition research experiment (fire) *Proc. 18th Int. Conf. on Fusion Energy 2002 (Sorrento, 2000)* (Vienna: IAEA) CD-ROM file, paper ftp2/16 and http://www.iaea.org/ programmes/ripc/physics/fec2000/html/node1.htm
[21] Coppi B., Airoldi A., Bombarda F., Cenacchia G., Detragiachea P. and Sugiyama L.E. 2001 *Nucl. Fusion* **41** 1253
[22] Airoldi A. and Cenacchi G. 2001 *Nucl. Fusion* **41** 687
[23] Airoldi A. and Cenacchi G. 1997 *Nucl. Fusion* **37** 1117
[24] Coppi B., Nassi M. and Sugiyama L.E. 1992 *Phys. Scr.* **45** 112
[25] Luxon J.L. and Davis L.G. 1985 *Fusion Technol.* **8** 441
[26] Rebut P.H. and Keen B.E. 1987 *Fusion Technol.* **11** 13
[27] Hutchinson I. *et al* 1994 *Phys. Plasmas* **1** 1511
[28] Waltz R.E., Candy J.M. and Rosenbluth M.N. 2002 *Phys. Plasmas* **9** 1938
[29] Jenko F., Dorland W., Kotschenreuther M. and Rodgers B.N. 2000 *Phys. Plasmas* **7** 1904
[30] Candy J. and Waltz R.E. 2003 *J. Commun. Phys.* **186** 545
[31] ITER Confinement Database and Modeling Expert Group 1999 *Nucl. Fusion* **39** 2137
[32] Thomsen K., Cordey J.G., the H-Mode Database Working Group and the Pedestal Database Working Group 2002 *Plasma Phys. Control. Fusion* **44** A429
[33] Kardaun O.J.W.F., the ITPA H-mode Database and P.D.W. Groups 2000 *Proc. 18th Int. Conf. on Fusion Energy 2002 (Sorrento, 2000)* (Vienna: IAEA) CD-ROM file, paper IAEA-CN-77/ITER/P-4 and http://www.iaea.org/ programmes/ripc/physics/fec2000/html/node1.htm
[34] Hatae T. *et al* 2001 *Nucl. Fusion* **41** 285
[35] Cordey J.G. and the JET Team 1999 *Nucl. Fusion* **39** 1763
[36] Onjun T., Bateman G., Kritz A.H. and Hammett G. 2002 Models for the pedestal temperature at the edge of H-mode tokamak plasmas *Phys. Plasmas* **9** 5018
[37] Kadomtsev B.B. 1975 *Sov. J. Plasma Phys.* **1** 295
[38] Cordey J.G., the ITPA H-mode Database and PDW Groups 2003 *Nucl. Fusion* **43** 670
[39] Bateman G., Onjun T. and Kritz A.H. 2003 *Plasma Phys. Control. Fusion* **45** 1939
[40] Hawryluk R.J. 1980 *Proc. Course in Physics of Plasmas Close to Thermonuclear Conditions (Varenna, 1979)* vol 1 (Brussels: Commission of the European Communities) p 19
[41] John H.E.S., Taylor T.S., Lin-Liu Y.-R. and Turnbull A.D. 1995 *Proc. 15th IAEA Fusion Energy Conf. on Plasma Physics and Controlled Nuclear Fusion Research (Seville, 1994)* vol 3 (Vienna: International Atomic Energy Agency) p 603
[42] Kim Y.B., Diamond P.H. and Groebner R.J. 1991 *Phys. Fluids* B **3** 2050
[43] Hirshman S.P. and Sigmar D.J. 1981 *Nucl. Fusion* **21** 1079
[44] Huba J.D. 2000 *NRL Plasma Formulary* Naval Research Laboratory, Washington, DC, p 20375
[45] Trubnikov B.A. 1972 *Sov. Phys.—JETP* **16** 25
[46] Singer C.E. *et al* 1988 *Comput. Phys. Commun.* **49** 275